Fast Response, Highly Sensitive and Selective Mixed-Potential H$_2$ Sensor Based on (La, Sr)(Cr, Fe)O$_{3-\delta}$ Perovskite Sensing Electrode

He Zhang[a], Jianxin Yi [a, *], Xi Jiang[b]

[a]*State Key Laboratory of Fire Science, Department of Safety Science and Engineering, University of Science and Technology of China, Hefei, Anhui, 230026, P.R. China*

[b]*School of Engineering and Materials Science, Queen Mary University of London, Mile End Road, London E1 4NS, United Kingdom*

ABSTRACT: A planar mixed-potential type sensor consisting of La$_{0.8}$Sr$_{0.2}$Cr$_{0.5}$Fe$_{0.5}$O$_{3-\delta}$ sensing electrode, yttria-stabilized zirconia solid electrolyte, and Pt reference electrode was developed for H$_2$ detection. The sensor showed high and repeatable response with a value of -143.6 mV for 1000 ppm H$_2$ at 450 ˚C. The sensor response varied linearly or logarithmically with the hydrogen concentration in the range of 20-100 ppm and 100-1000 ppm H$_2$, respectively. The response/recovery time generally decreased with increasing concentration and temperature, and reached almost steady above 300 ppm H$_2$. Response time as short as 4 s and recovery time of 24 s were attained at 450 ˚C for 500 ppm. The sensor exhibited excellent selectivity to hydrogen against interference of CH$_4$, C$_3$H$_8$, CO, NO$_2$, and NH$_3$. The mixed-potential mechanism was assessed by electrochemical measurements, and the sensing behavior was discussed in relation to the reaction kinetics. The excellent H$_2$ sensing performance for concentrations above 100 ppm is ascribed to the high electrocatalytic activity of the perovskite electrode to H$_2$ oxidation. The inferior performance for

lower H_2 concentrations may be related with slow gas diffusion in the electrode.

KEYWORDS: *Perovskite, mixed-potential, H_2 sensor, electrochemical, sensing mechanism.*

1. INTRODUCTION

As a clean and renewable fuel, hydrogen has been widely used in many fields such as chemical industry and aerospace.[1-3] However, hydrogen is also a highly combustible gas with a particularly low ignition energy (0.02 mJ) and wide range of explosive limit (4%~74% in air).[4] It cannot be merely sensed by human beings due to the colorless, odorless, and tasteless nature. For safety's sake, it is thus of crucial importance to detect and monitor the hydrogen concentration in the usage and storage places. Among many techniques developed for gas detection so far, H_2 gas sensor has been considered as one effective approach for real-time monitoring of H_2.[2,4]

Mixed-potentiometric H_2 sensors have attracted great attention due to the robustness, simple support electronics, and high stability.[5-7] Typically operated at a temperature above 350-400 ˚C, this type of sensors holds potentials especially for applications involving H_2 at high temperatures, e.g., ammonia production and H_2 production via methane reforming. The sensor generally consists of a solid electrolyte such as yttria-stabilized zirconia, a sensing electrode, and a reference electrode. It responds to the analyte gases by changes in the electrode potential, which is generated from the various electrochemical reactions occurring at the electrode/electrolyte

interface.[8-10] According to the mixed-potential theory, the sensor response is significantly governed by the property of the sensing electrode material such as type and morphology.[11] As a result, much effort has been devoted to exploring high performance sensing electrode material during the past decades. Lu et al. reported a tubular sensor attached with ZnO sensing electrode, which showed good response to hydrogen at 600 ˚C.[10] Anggraini et al. found that a sensor with composite sensing electrode of 10 wt.% Au and $ZrSiO_4$ exhibited excellent selectivity to hydrogen.[9] Martin et al. found that a sensor with Sn-doped In_2O_3 as sensing electrode displayed fast response to hydrogen in air.[12] Nonetheless, few state-of-the-art sensors meet all the important criteria for practical applications, such as high sensitivity, good selectivity, and fast response speed. Meanwhile, previous selection of the sensing electrode materials was usually based on an empirical trial and error approach, and a more rational strategy is demanded.

The sensing response of mixed-potential sensors depends greatly on the electrocatalytic activity of the sensing electrode. Materials with high electrochemical activity to hydrogen oxidation and in the meantime low activity to oxygen reduction are in principle beneficial to the H_2 sensing property.[11] Perovskite-structured oxides possess tunable electrocatalytic activity towards these reactions, depending on the diverse composition, and have thus been widely studied in gas sensors,[13] solid oxide fuel cells,[14-16] and oxygen separation membranes.[17] Fe-doped (La, Sr)$CrO_{3-\delta}$ perovskite oxide exhibited low polarization resistance as the anode material of solid oxide fuel cell operated in H_2 fuel,[14,15] suggesting that it is highly active for H_2

electrochemical oxidation. Moreover, $La_{0.8}Sr_{0.2}Cr_{0.5}Fe_{0.5}O_{3-\delta}$ (LSCF) possesses excellent chemical stability and compatibility with yttria-stabilized zirconia even at temperatures up to 1430 ˚C.[18,19] Therefore, this material may also be a potential candidate for the sensing electrode of a mixed-potential H_2 sensor.

In this work, a planar mixed-potential sensor was constructed, using LSCF as sensing electrode, $Zr_{0.84}Y_{0.16}O_{1.92}$ (YSZ) and Pt as solid electrolyte and reference electrode, respectively. The sensing performance of the sensor was systematically studied, and the sensing behavior and mechanism was also discussed.

2. EXPERIMENTAL

2.1. Sensor preparation and characterization

Commercial YSZ powders, which were obtained by co-precipitation and calcination at 1100 ˚C for 24 h, were purchased from Yiming Materials Technology, China. LSCF powders synthesized via a sol-gel route with calcination at 700 ˚C for 3 h were provided by Ruier Chemical Technology, China. To obtain disk-shaped YSZ solid electrolyte, the YSZ powders were subject to uniaxial pressing at a pressure of 218 MPa followed by sintering at 1400 ˚C for 10 h. A paste of LSCF powder and organic binder (α-terpineol and ethyl cellulose) in a 1:1 wt. ratio was then coated on the YSZ disk, and sintered at 1000 ˚C for 3 h to obtain the sensing electrode (SE). Two Pt pastes (Sino-Platinum Co., Ltd., China) were coated on the same side of the YSZ disk and sintered at 800 ˚C for 10 min, serving as the reference electrode (RE) and counter electrode (CE), respectively. Each of the three electrodes had a diameter

of 2.7 mm and the spacing between each other was ~5.6 mm. A Pt wire was attached to each electrode with some high temperature silver paste (DAD-87, Shanghai Research Institute of Synthetic Resins, China) after dried at 200 ˚C for 2 hours. The Pt wires were used for collecting the electric signals.

Crystal structure and phase composition of the powders were characterized by an X-ray diffractometer (Rigaku TTR-Ⅲ) using Cu Kα radiation. The morphologies of SE and RE were analyzed by using scanning electron microscopy (SEM, JEOL JSM-6700F) operated at an accelerating voltage of 20 kV. Quantitative elemental analysis was conducted with X-ray fluorescence spectrometry (XRF-1800, Shimadzu).

2.2. Sensor test

Sensing and electrochemical measurements were performed using a home-built setup schematically shown in Figure 1. The sensor was placed in a quartz tube located in an electric furnace. Sample gas of desired concentration was obtained by mixing dry air and certified gas containing the respective analyte gas (H_2, NO_2, CH_4, C_3H_8, CO, NH_3) and N_2 as balance gas. The gas flow rates were regulated with mass flow controllers (MFC, CS200, Beijing Sevenstar Electronics, China), and the total flow rate was fixed at 100 ml/min (400-450 ˚C) or 200 ml/min (500 ˚C, 550 ˚C). For characterizing the sensing characteristics, a two-electrode configuration was employed, with the positive and negative terminal of the electrometer connected to the SE and RE, respectively. A digital electrometer (Agilent, 34461A) was used to measure the electromotive force (EMF) of the sensor. Response of the sensor was

defined as $\Delta EMF = EMF_{gas} - EMF_{air}$, where EMF_{gas} and EMF_{air} represent the EMF of the sensor in sample gas and in air, respectively. Response/recovery time of the sensor was defined as the time for the sensor response to achieve 90% of the ΔEMF change upon feeding/removal of H_2. The polarization curves and AC impedance spectra were measured using an electrochemical workstation (CHI604E, Chenhua, China) with a three-electrode configuration. In this case, the CE was also connected to form a current conduction circuit with the SE to avoid polarization of the SE. The polarization curves were tested by means of potentiodynamic method under a scan rate of 0.5 mV/s. The complex impedance measurements were performed at a fixed amplitude of 5 mV in a frequency range from 0.1 Hz to 1 MHz.
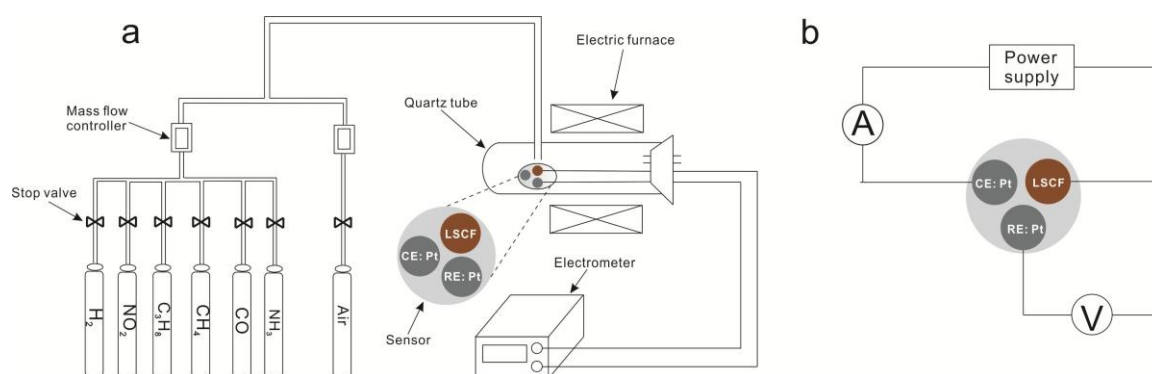

Figure 1. Schematic illustration for the (a) sensor test rig and (b) principle of electrochemical measurements.

3. Results and discussion

3.1. Materials properties and microstructure

As revealed by XRF, the atomic metal compositions of the as-received LSCF and YSZ powders were La : Sr : Cr : Fe = 0.79 : 0.21 : 0.48 : 0.52 and Zr : Y = 0.86 : 0.14,

respectively, which matched very well with the nominal ones. As shown in Figure 2, single phase fluorite structured YSZ (JCPDS No.: 3-640) and orthorhombic LSCF (JCPDS No.: 1-75-441) were obtained after sintering at 1400 ˚C and 1000 ˚C, respectively. SEM images in Figure 3 showed that both the LSCF SE and Pt RE were highly porous, which would be beneficial to the gas transport during the sensing measurements. The thickness of the SE and RE was 70 μm and 50 μm, respectively. The particle size of LSCF was typically in the range of 100~200 nm.
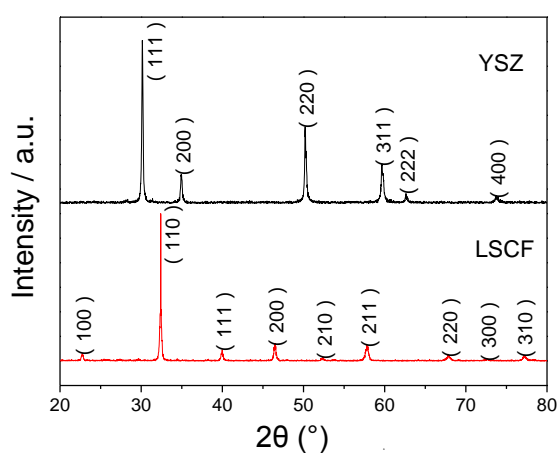

Figure 2. XRD patterns of YSZ electrolyte and LSCF electrode after sintering.
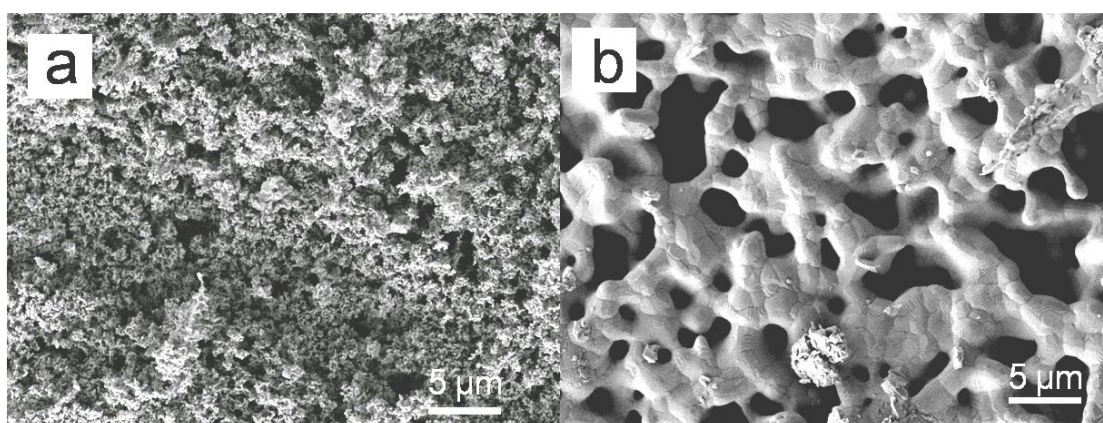

Figure 3. Surface SEM images of (a) sensing electrode and (b) reference electrode.
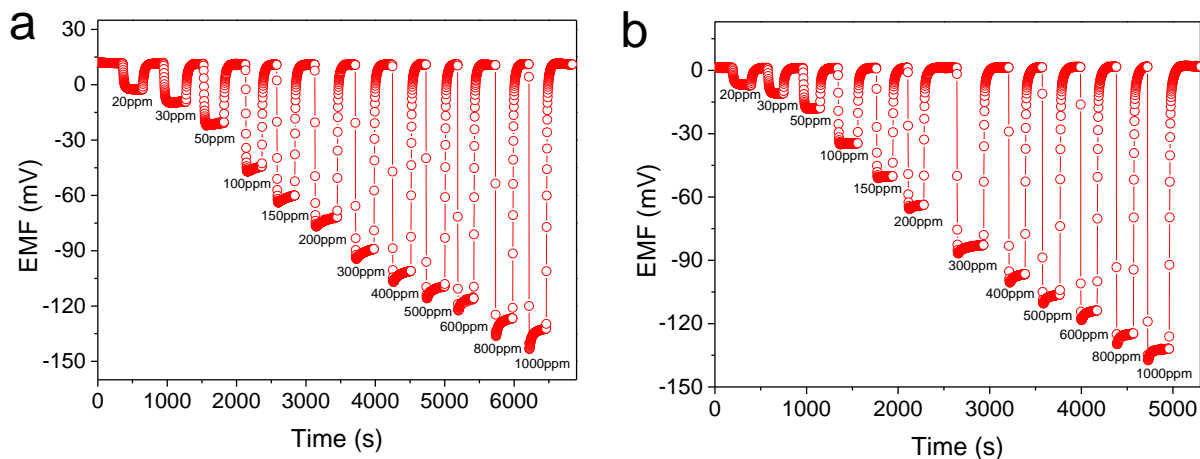
3.2. Sensing properties

Figure 4. Response and recovery transients of the LSCF/YSZ/Pt sensor in different concentrations of hydrogen at (a) 450 °C and (b) 500 °C.

Figure 4 shows representative response and recovery transients of the LSCF/YSZ/Pt sensor. Positive EMF baselines were observed in air, which decreased with increasing temperature. The none-zero EMF resulted from the different electrochemical activity for the cathodic reduction of O_2 for the LSCF SE and Pt RE. Upon exposure of the sensor to hydrogen-containing atmosphere, negative EMF values were observed, which became more negative with increase of H_2 concentration. As the atmosphere was switched back to air, the EMF could rapidly restore to the initial baseline. Note that in some cases, a spike appeared before the potential reached the plateau value upon introduction of H_2, which has similarly been observed by others[3,20]. The spike appeared to become more pronounced at lower temperatures and higher H_2 concentrations, implying that it may be related with the reaction kinetics. It is likely that at the early stage of the sensing upon H_2 introduction, the relevant reactions had not reached the steady state, giving rise to the occurrence of this

8

phenomenon. In the present work, the plateau EMF values following the spike were used for calculation of the response and the response/recovery time to avoid disturbance of the spike.

Figure 5 shows the response (ΔEMF) of the LSCF/YSZ/Pt sensor as a function of H_2 concentration in the temperature range of 400 ˚C -550 ˚C. The sensor response generally increased, i.e., became more negative, with increasing H_2 concentration. At 450 ˚C, a high response of -55.4 mV and -143.6 mV was achieved for 100 ppm and 1000 ppm H_2, respectively. For H_2 concentration below 100 ppm, the response was found to vary linearly with the H_2 concentration. Slope of the linear fitting, which was normally used to represent the sensitivity of the sensor, decreased monotonously with increasing temperature. In contrast, the response varied linearly with the logarithmic H_2 concentration for concentrations above 100 ppm. The slope of the linear fitting first increased with the temperature, and then decreased again above 500 ˚C. A maximum sensitivity of -101.2 mV/decade appeared at 500 ˚C, and a slightly smaller sensitivity, -90.0 mV/decade, was obtained at 450 ˚C. The different dependence of sensor response on the analyte gas concentration in low and high concentration ranges, which has similarly been observed for other sensors,[21] is indicative of different sensing mechanism according to the mixed-potential theory.[21,22] A linear H_2 concentration dependence of the mixed potential suggests that the oxygen reduction kinetics follows the low overpotential linear approximation of the Butler-Volmer equation, and that in the meantime the H_2 oxidation kinetics is rate-limited by the diffusional mass transport. By contrast, the logarithmic concentration dependence of

the mixed potential in the high concentration range suggests that Tafel-type kinetics applied to either or both of the anodic and cathodic reactions.
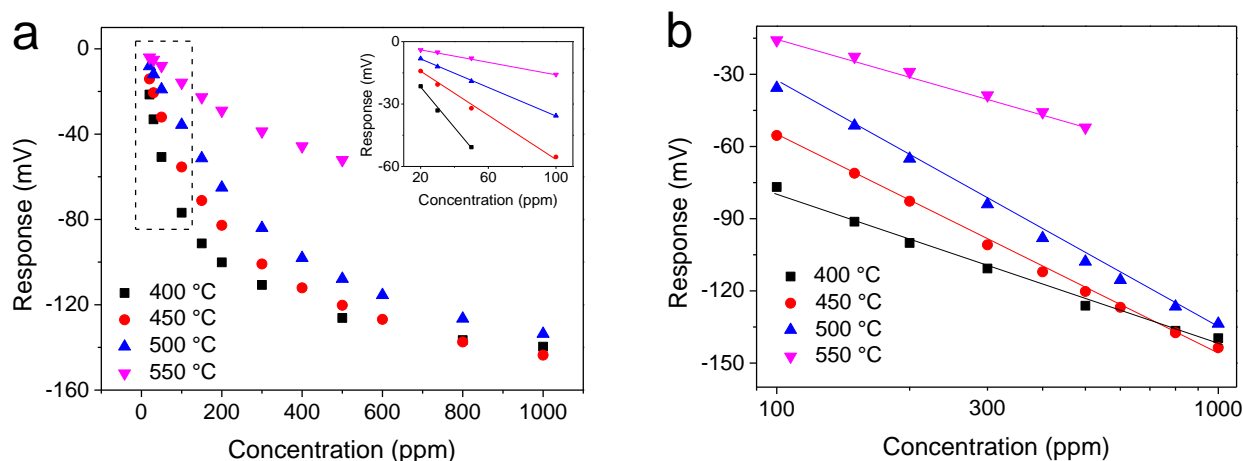

Figure 5. Response of LSCF/YSZ/Pt sensor as a function of hydrogen concentration on a (a) linear scale, (b) logarithmic scale. Inset in (a) is a zoom of the marked rectangle area. Solid lines are guide to the eye.

Figure 6 displays the response/recovery time for the sensor as a function H_2 concentration. The response time, which was around several tens of seconds at low H_2 concentrations (below 100 ppm), decreased quickly with increasing hydrogen concentration and slightly with increasing temperature, and approached to an almost constant value above ~300 ppm. The response time for 500 ppm H_2 was as short as 4 s and 3 s at 450 ˚C and 550 ˚C, respectively. Moreover, a linear relationship between the response time and reciprocal concentration was observed for the data of 100-1000 ppm. Similarly, the recovery time also exhibited a decreasing trend and a plateau with concentration increasing (except at 400 ˚C). Nonetheless, no linear relationship

between it and the reciprocal concentration was found. The recovery time for 500

ppm H_2 was as short as 10 s at 550 °C, which increased remarkably to 20 s, 24 s, and

164 s as temperature was decreased to 500 °C, 450 °C and 400 °C, respectively. Note

that at the lowest temperature, 400 °C, the recovery time exhibited a concentration

dependence opposite to that observed at higher temperatures, that is, it increased with

the concentration prior to reaching the plateau. Taking into account the requirements

for high response values, fast response/recovery speed, and safety (best operated at a

temperature below 500-585 °C, the auto-ignition temperature of H_2), these results

suggest an optimum operation temperature at 450 °C for the LSCF/YSZ/Pt sensor.
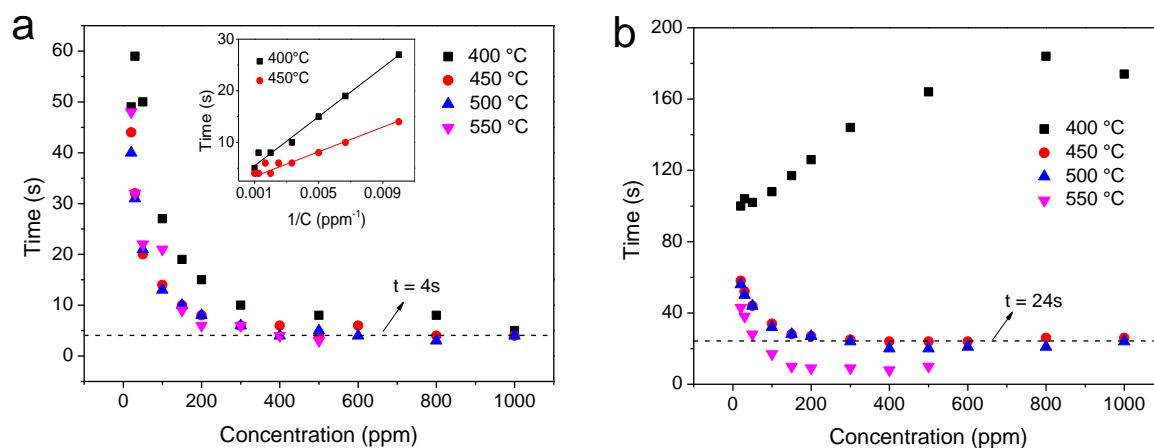

Figure 6. Variation of (a) response time and (b) recovery time with hydrogen

concentration. Inset in (a) shows the response time versus reciprocal hydrogen

concentration in the range of 100-1000 ppm, where solid lines are guide to the eye.

The selectivity of the LSCF/YSZ/Pt sensor, an important parameter for

evaluating a gas sensor's performance, was assessed by comparing its response to 100

ppm different gases at 450 °C. As shown in Figure 7, the absolute values of the

response decreased in the order of $H_2 \gg CO > NO_2 \sim C_3H_8 \gg CH_4 \sim NH_3$. The response to H_2 was over 4.5 times higher than that to CO, the most responsive interferent, indicating that the sensor is highly selective to H_2.
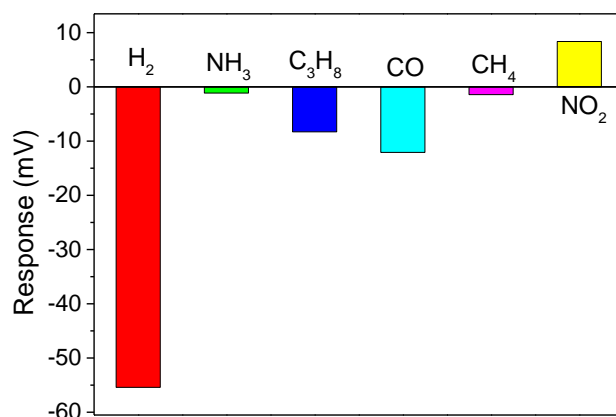

Figure 7. Cross sensitivities for the LSCF/YSZ/Pt sensor to 100 ppm various gases at 450 ℃
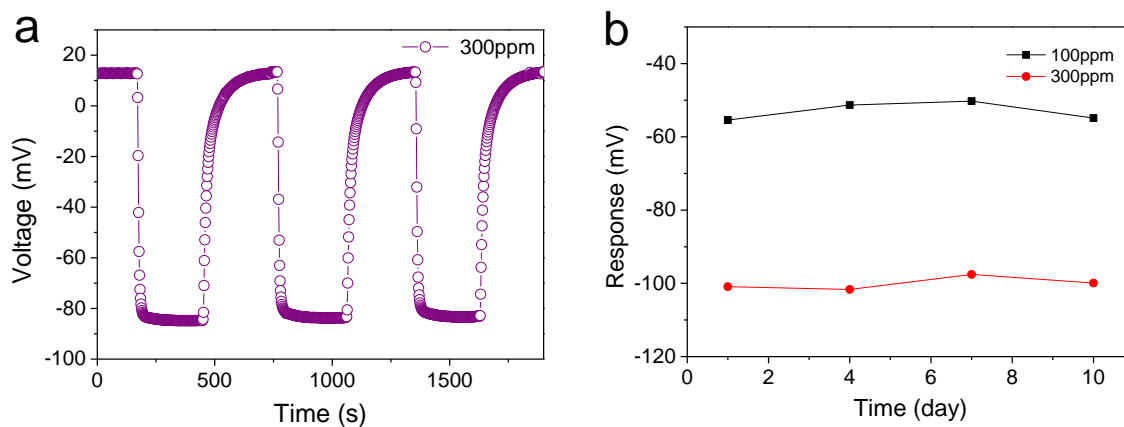

Figure 8. (a) Continuous dynamic response and (b) long-term stability of the sensor at 450 ˚C.

Figure 8a shows that during a continuous three-cycle measurement in 300 ppm H_2 at 450 ˚C, the dynamic response and recovery process of the sensor was well

repeated. Figure 8b indicates that the sensor was successfully operated for 10 days at 450 °C and did not exhibit any significant variation or decay in the response to 100 ppm and 300 ppm H_2. These results demonstrated good repeatability and long-term stability of the sensor performance.

3.3. Electrochemical processes

In order to explore the reaction mechanism, polarization curves of a separate LSCF/YSZ/Pt sensor were measured at 450 °C in air or in the H_2 concentration range of 100 ppm-800 ppm. As shown in Figure 9, the cathodic current (in absolute values) measured in air varied almost linearly with the applied potential. This behavior agrees well with the low overpotential linear approximation of the Butler-Volmer equation, and excludes the Tafel-type kinetics for the cathodic oxygen reduction reaction.[11, 23] The modified anodic polarization curves were obtained by subtracting the current values measured in air from those obtained in H_2-containing atmospheres. It can be seen that the anodic current increased with increasing H_2 concentration, and also varied linearly with the potential. In combination with the linear oxygen reduction kinetics and the logarithmic H_2 concentration dependence of the response in this concentration range, this suggests electrochemical reaction, most likely of Tafel-type kinetics, as the rate-limiting step for the anodic process.[23] In addition, the possibility of a gas diffusion-controlled process can also be excluded. The intersection of the modified anodic polarization curve with the cathodic curve corresponds to the equilibrium of the anodic and cathodic reaction. The ΔEMF calculated from the

13

polarization curves was found to agree well with the measured sensor response for each H_2 concentration (Table 1). This observation clearly demonstrates that sensing of the LSCF/YSZ/Pt sensor followed the mixed-potential mechanism.
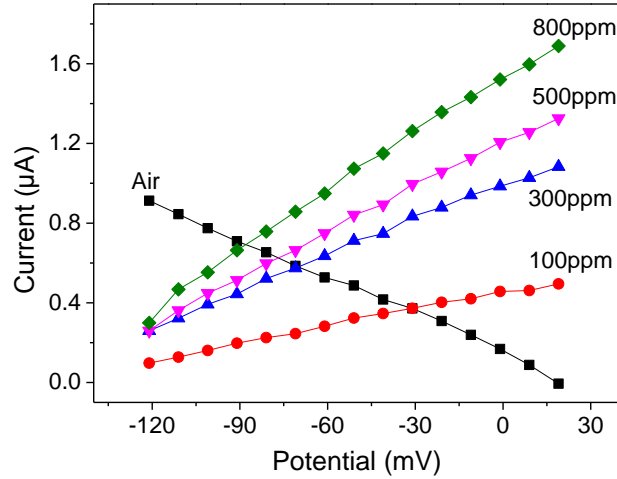

Figure 9. Modified polarization curves for a separate LSCF/YSZ/Pt sensor at 450 ˚C.

Table 1. Comparison of the calculated and measured ΔEMF for the sensor at 450 ˚C

Concentration (ppm)	100	300	500	800
Calculated (mV)	-50.3	-89.9	-101.8	-110.5
Measured (mV)	-50.5	-89.5	-95.7	-106.6

To gain more insight into the electrochemical process for the sensor, electrochemical impedance spectroscopy was also performed. As shown in Figure 10, two arcs can be observed in the Nyquist plots obtained in air atmosphere containing 100 ppm-800 ppm H_2. The intercept of the high frequency arc with the real axis corresponds to the ohmic resistance (R_o) of the device, and that of the low frequency

represents the total resistance (R_t). The difference between R_t and R_o is the resistance of the interface between the electrolyte and electrode, R_i. The fitted R_o and R_i values were plotted versus H_2 concentration (C_{H_2}) in Figure 11. It can be seen that both R_o and R_i decreased significantly with increasing temperature. At a given temperature, R_o was almost invariant regardless of the H_2 concentration. On the contrary, R_i was sensitive to the presence of H_2, and decreased monotonically with increasing C_{H_2}. This trend is consistent with the increasing response of the sensor. A linear relation was observed for the log-log plots of R_i versus C_{H_2} at different temperatures. The power law-type dependence, $R_i \propto C_{H_2}^n$, was obtained with n= -0.45, -0.31, and -0.16 at 450 ˚C, 500 ˚C, and 550 ˚C, respectively. Similar power law dependence of anodic polarization resistance on the H_2 partial pressure has been observed in several studies on solid oxide fuel cells.[14,24] According to the model Zhu et al. developed, a power law exponent of -1 corresponded to dissociative adsorption of H_2 as the rate-limiting step, whilst a value of -0.5 corresponded to the charge-transfer reaction limit.[24] If this model also holds for the present case, the much smaller n value obtained here relative to -1 would exclude a significant role of gas diffusion or dissociative adsorption limit. The observation that the n value was very close to -0.5 at 450 ˚C thus suggests the anodic process may be rate-limited by the charge-transfer reaction. This is also consistent with the results of sensor response and polarization curve measurements in Figure 5b and Figure 9. Nevertheless, it is noteworthy that the activity of LSCF to the cathodic oxygen reduction reaction as well as to the heterogeneous oxidation of hydrogen, which may also play a significant role in governing the electrochemical

behavior of the sensor,[9] still remains unclear. Further investigation is needed in order to shed more light on the detailed reaction mechanism.
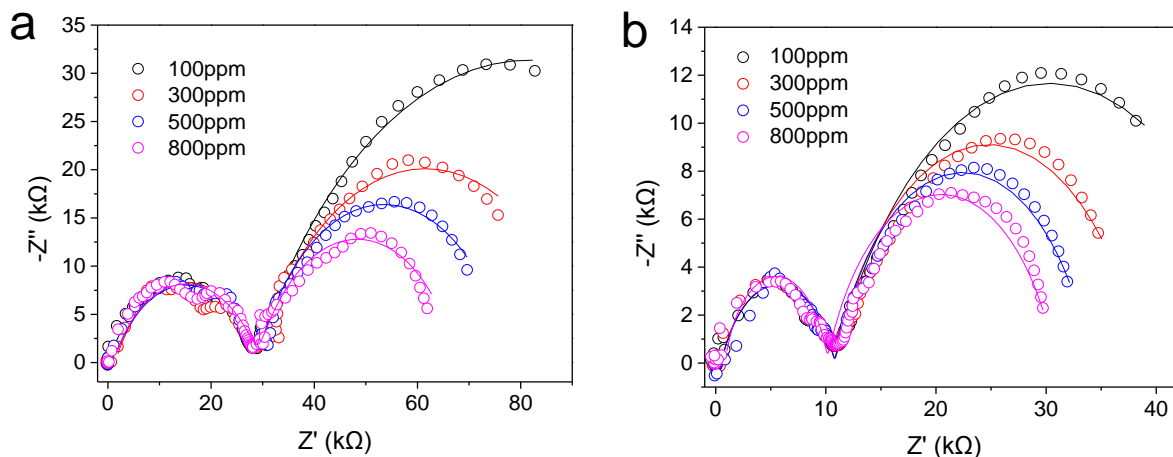

Figure 10. Nyquist plots (symbols) and corresponding fits (solid lines) at (a) 450 ˚C and (b) 500 ˚C.
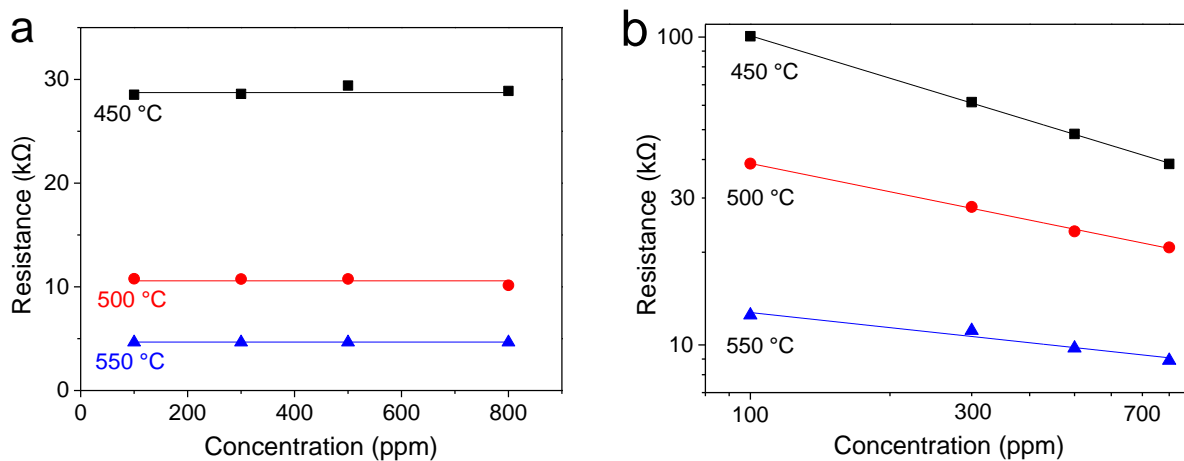

Figure 11. (a) Ohmic resistance and (b) interfacial resistance of the sensor versus hydrogen concentration at various temperatures.

3.4. Relation of sensing behavior and reaction kinetics

The response of mixed potential sensors depends on the kinetics of various

electrochemical and heterogeneous reactions taking place at the electrode/electrolyte interface and at the electrode surface.[11, 23] The results obtained in this work clearly reveal that the LSCF/YSZ/Pt sensor adopted different sensing mechanisms for H_2 concentrations below and above 100 ppm (Figure 5). In the higher H_2 concentration regime, operation of the LSCF/YSZ/Pt sensor was rate-limited by the Tafel-type kinetics of the electrochemical reactions at the LSCF/YSZ interface. Therefore, the high H_2 sensitivity of the sensor can be attributed to the high electrochemical activity to H_2 oxidation of LSCF, which favors fast reaction kinetics. The much lower electrochemical activity to methane oxidation than to H_2 oxidation for LSCF, which has been revealed in the SOFC studies,[16, 25] is consistent with the poor methane response of the sensor in Figure 7. Therefore, the high H_2 selectivity of the LSCF/YSZ/Pt sensor may stem from the superior electrochemical activity of LSCF to H_2.

Similarly, the response/recovery speed of the sensor in the higher H_2 concentration regime would also be connected with the kinetics of the electrochemical reactions. To gain more insight into this relationship, the mechanism and kinetics of H_2 oxidation reaction are discussed as follows. The overall H_2 oxidation reaction

$$H_2(g) + O^{2-} \rightarrow H_2O(g) + 2e^- \tag{1}$$

generally consists of three steps, H_2 adsorption/desorption, oxidation reaction, and H_2O desorption/adsorption.[24]

$$H_2(g) \underset{k_{-1}}{\overset{k_1}{\rightleftharpoons}} H_2(ads) \tag{2}$$

$$H_2(ads) + O^{2-} \xrightarrow{k_2} H_2O(ads) + 2e^- \tag{3}$$

$$H_2O(ads) \xrightleftharpoons[k_{-2}]{k_2} H_2O(g) \tag{4}$$

In these expressions, (g) denotes gas phase and (ads) denotes adsorbed at the LSCF/YSZ interface, and for simplicity H_2 dissociation is not discussed here. Assuming that both adsorption/desorption of H_2 and H_2O take place very rapidly and thus equilibrium for Reaction 2 and 4 can be established, the overall reaction would be rate-limited by the surface reaction, Reaction 3. According to the Langmuir Adsorption Isotherm[26], the overall reaction rate can be expressed as

$$r = k_2[O^{2-}]\theta_{H_2} = \frac{k_2[O^{2-}]a_{H_2}p_{H_2}}{1 + a_{H_2}p_{H_2} + a_{H_2O}p_{H_2O}} \tag{5}$$

where symbols have their usual meaning. Under the conditions in the present work, the oxygen partial pressure and the H_2O partial pressure (p_{H_2O}) is basically constant in the feed gas. Correspondingly, a fixed concentration of oxide ions, $[O^{2-}]$, will be attained at the LSCF/YSZ interface. According to Equation 5, the reaction rate (r) will increase with the H_2 partial pressure (p_{H_2}), and then approach to a limiting/constant value. Moreoever, a linear relation between their reciprocals, $r^{-1} \propto p_{H_2}^{-1}$, can be obtained. This relation coincides well with that for the response time and the reciprocal H_2 concentration (Figure 6a), suggesting a reciprocal relationship between the reaction rate and the response time. Therefore, the response time of the sensor in the Tafel regime is most likely also governed by the kinetics of the electrochemical reactions. The observed short response time indicates fast reaction kinetics, which also matches well with the good electrocatalytic activity of LSCF to H_2 oxidation. In contrast, upon removal of H_2 from the feed gas during the recovery process, the H_2 adsorption (forward Reaction 2) and thus Reaction 3 are terminated, while the H_2

desorption (backward Reaction 2) and Reaction 4 remain. The kinetics of the recovery process may then be dominated by that of H_2 desorption as p_{H_2O} is constant. It may also be reasonable to speculate that high desorption rate would lead to a short recovery time, in a similar way to a high reaction rate versus short response time. The concentration variation of the recovery time may find its origin from the desorption rate. The H_2 desorption rate at the beginning of recovery can be calculated by

$$r = k_{-1}\theta_{H_2} = \frac{k_{-1}a_{H_2}p_{H_2}}{1 + a_{H_2}p_{H_2} + a_{H_2O}p_{H_2O}} \tag{6}$$

which increases with the H_2 partial pressure. However, the desorption rate is not constant and will decrease quickly with time in the absence of H_2, which prevents further analysis of the recovery process. Despite that the concentration profile of the recovery time resembles that of the response time (Figure 6), different reaction kinetics and mechanisms would be expected due to the different reaction pathways.

The temperature dependence of the response/recovery time in Figure 6 can in principle be explained as a result of an increased reaction/desorption rate at higher temperatures. The distinctly different concentration dependence of the recovery time for 400 ˚C and 450 ˚C in Figure 6b implied that probably a threshold temperature was present between 400-450 ˚C. Below this temperature, desorption may become much more difficult, leading to a longer recovery time and different behavior at 400 ˚C.

At low H_2 concentrations (below 100 ppm), diffusion-limited kinetics was observed for the LSCF/YSZ/Pt sensor. This behavior indicates that as compared with the rapid electrocatlytic H_2 oxidation reaction, the gas diffusion through the pores in the electrodes was slow, which accounts for the much longer response/recovery time

(Figure 6). Meanwhile, insufficient amount of H_2 reached the LSCF/YSZ interface, giving rise to rapid linear decay of the sensor response with decreasing H_2 concentration (Figure 5a). Therefore, better sensing performance, e.g., higher sensitivity and faster response/recovery speed, could likely be achieved by optimization of the electrode microstructure enabling fast gas transport.

Table 2. A summary of the sensing performance of state-of-the-art mixed-potential hydrogen sensors with different SE (SE/YSZ/Pt).

SE	Temperature (°C)	Concentration (ppm)	Response* (mV)	Response / recovery time (s)	Reference
CuO-ZnO-Al$_2$O$_3$	430	107	9	150/ 900	27
ZnO	600	50	75	5 / 10	10
ITO	535	5000	135~167	3~7 / -	3
Au-mesh	550	100	180	83 / 69	28
Cr$_2$O$_3$/Al$_2$O$_3$/SnO$_2$(+YSZ)	550	100	70	10 / 30	29
ZnO(+Ta$_2$O$_5$)	500	100	600	70 / -	21
ZnWO$_4$	600	30000	180	60 / 60	20
ZrSiO$_4$(+Au)	500	100	25	11 / 21	9
MnWO$_4$	500	960	110	95 / 160	30
CdWO$_4$	500	30000	270	35 / 90	31
LSCF	450	100	55	14 / 34	This work
LSCF	500	100	37	13 / 32	This work
LSCF	500	1000	134	4 / 24	This work

*: absolute values

For practical applications, gas sensors are required to simultaneously possess fast response/recovery rate, sufficient sensitivity, as well as a high selectivity and stability. As compared with state-of-the-art mixed-potential hydrogen sensors (Table 2), the LSCF/YSZ/Pt sensor studied in this work exhibited an excellent balance between fast response/recovery speed and high response. The very short response time obtained at 450 °C, a temperature well below the auto-ignition temperature of H_2, is a particular

advantage and of crucial significance for real-time monitoring of this highly explosive gas. Moreover, its good selectivity to hydrogen against common interferent gases as well as the good stability is an extra bonus. These features are strongly correlated with the prominent electrocatalytic activity of the SE material, LSCF. The results obtained here may help rationalize future development of mixed-potential type sensors.

4. Conclusion

The planar $La_{0.8}Sr_{0.2}Cr_{0.5}Fe_{0.5}O_{3-\delta}$/YSZ/Pt sensor exhibited high and repeatable response to H_2, achieving -55.4 mV for 100 ppm and -143.6 mV for 1000 ppm H_2 at 450 °C. The sensor response varied linearly or logarithmically with the hydrogen concentration in the range of 20-100 ppm and 100-1000 ppm, respectively. The response time decreased with hydrogen concentration, and reached almost steady above 300 ppm H_2. Similar behavior was also observed for the recovery time at 450 °C and above. Response time of 4 s and recovery time of 24 s were attained for 500 ppm at 450 °C. The sensor exhibited only minor cross sensitivity towards C_3H_8, CO, and NO_2, and negligible response to CH_4 and NH_3, indicating excellent hydrogen selectivity. The sensing behavior could be well interpreted by the mixed-potential theory. The excellent performance of the sensor for H_2 concentration above 100 ppm is linked with the good electrochemical activity of $La_{0.8}Sr_{0.2}Cr_{0.5}Fe_{0.5}O_{3-\delta}$ to the H_2 oxidation reaction. The inferior performance for low H_2 concentrations can be attributed to the slow gas diffusion in the SE electrode.

AUTHOR INFORMATION

Corresponding Author

* E-mail address: yjx@ustc.edu.cn.

Telephone: +86 551 63607817

ACKNOWLEDGEMENTS

REFERENCES

(1) Verhelst, S.; Wallner, T. Hydrogen-Fueled Internal Combustion Engines. *Prog. Energy Combust. Sci.* **2009,** *35*, 490-527.

(2) Buttner, W. J.; Post, M. B.; Burgess, R.; Rivkin, C. An Overview of Hydrogen Safety Sensors and Requirements. *Int. J. Hydrogen Energy* **2011,** *36*, 2462-2470.

(3) Sekhar, P. K.; Brosha, E. L.; Mukundan, R.; Nelson, M. A.; Williamson, T. L.; Garzon, F. H. Development and Testing of a Miniaturized Hydrogen Safety Sensor Prototype. *Sens. Actuators, B* **2010,** *148*, 469-477.

(4) Hübert, T.; Boon-Brett, L.; Black, G.; Banach, U. Hydrogen Sensors-A Review. *Sens. Actuators, B* **2011,** *157*, 329-352.

(5) Ramamoortyy, R.; Dutta, P. K.; Akbar, S. A. Oxygen Sensors: Materials,

Methods, Desigens and Applications. *J. Mater. Sci.* **2003,** *38*, 4271-4282.

(6) Anggraini, S. A.; Breedon, M.; Miura, N. Zn-Ta-Based Oxide as a Hydrogen Sensitive Electrode Material for Zirconia-Based Electrochemical Gas Sensors. *Sens. Actuators, B* **2013,** *187*, 58-64.

(7) Anggraini, S. A.; Breedon, M.; Ikeda, H.; Miura, N. Insight into the Aging Effect on Enhancement of Hydrogen-Sensing Characteristics of a Zirconia-Based Sensor Utilizing a Zn-Ta-O-Based Sensing Electrode. *ACS Appl. Mater. Interfaces* **2013,** *5*, 12099-12106.

(8) Wang, B.; Liu, F. M.; Yang, X.; Guan, Y. H.; Ma, C.; Hao, X. D.; Liang, X. S.; Liu, F. M.; Sun, P.; Zhang, T.; Lu, G. Y. Fabrication of Well-Ordered Three-Phase Boundary with Nanostructure Pore Array for Mixed Potential-Type Zirconia-Based NO_2 Sensor. *ACS Appl. Mater. Interfaces* **2016,** *8*, 16752-16760.

(9) Anggraini, S. A.; Ikeda, H.; Miura, N. Tuning H_2 Sensing Performance of Zirconia-Based Sensor using $ZrSiO_4$(+Au) Sensing-Electrode. *Electrochim. Acta* **2015,** *171*, 7-12.

(10) Lu, G. Y.; Miura, N.; Yamazoe, N. High Temperature Hydrogen Sensor Based on Stabilized Zirconia and a Metal Oxide Electrode. *Sens. Actuators, B* **1996,** *35-36*, 130-135.

(11) Miura, N.; Sato, T.; Anggraini, S. A.; Ikeda, H.; Zhuiykov, S. A Review of Mixed-Potential Type Zirconia-Based Gas Sensors. *Ionics* **2014,** *20*, 901-925.

(12) Martin, L. P.; Pham, A. Q.; Glass, R. S. Electrochemical Hydrogen Sensor for Safety Monitoring. *Solid State Ionics* **2004,** *175*, 527-530.

(13) Tho, N. D.; Huong, D. V.; Ngan, P. Q.; Thai, G. H.; Thu, D. T. A.; Thu, D. T. et al. Effect of Sintering Temperature of Mixed Potential Sensor $Pt/YSZ/LaFeO_3$ on Gas Sensing Performance. *Sens. Actuators, B* **2016**, *224*, 747-754.

(14) Fowler, D. E.; Messner, A. C.; Miller, E. C.; Slone, B. W.; Barnett, S. A.; Poeppelmeier, K. R. Decreasing the Polarization Resistance of $(La,Sr)CrO_{3-\delta}$ Solid Oxide Fuel Cell Anodes by Combined Fe and Ru Substitution. *Chem. Mater.* **2015,** *27*, 3683-3693.

(15) Fowler, D. E.; Haag, J. M.; Boland, C.; Bierschenk, D. M.; Barnett, S. A.; Poeppelmeier, K. R. Stable, Low Polarization Resistance Solid Oxide Fuel Cell Anodes: $La_{1-x}Sr_xCr_{1-x}Fe_xO_{3-\delta}$ (x=0.2–0.67). *Chem. Mater.* **2014,** *26*, 3113-3120.

(16) Tao, S. W.; Irvine, J. T. S. Catalytic Properties of the Perovskite Oxide $La_{0.75}Sr_{0.25}Cr_{0.5}Fe_{0.5}O_{3-\delta}$ in Relation to its Potential as a Solid Oxide Fuel Cell Anode Material. *Chem. Mater.* **2004,** *16*, 4116-4121.

(17) Yi, J. X.; Schroeder, M.; Martin, M. CO_2-Tolerant and Cobalt-Free $SrFe_{0.8}Nb_{0.2}O_{3-\delta}$ Perovskite Membrane for Oxygen Separation. *Chem. Mater.* **2013,** *25*, 815-817.

(18) Yuan, R. H.; He, W.; Zhang, Y.; Gao, J. F.; Chen, C. S. Preparation and Characterization of Supported Planar $Zr_{0.84}Y_{0.16}O_{1.92}$-$La_{0.8}Sr_{0.2}Cr_{0.5}Fe_{0.5}O_{3-\delta}$ Composite Membrane. *J. Membr. Sci.* **2016,** *499*, 335-342.

(19) Liu, J. J.; Liu, T.; Wang, W. D.; Gao, J. F.; Chen, C. S. $Zr_{0.84}Y_{0.16}O_{1.92}$-$La_{0.8}Sr_{0.2}Cr_{0.5}Fe_{0.5}O_{3-\delta}$ Dual-Phase Composite Hollow Fiber Membrane Targeting Chemical Reactor Applications. *J. Membr. Sci.* **2012,** *389*,

435-440.

(20) Tang, Z. Y.; Li, X. G.; Yang, J. H.; Yu, J.; Wang, J.; Tang, Z. N. Mixed Potential Hydrogen Sensor Using ZnWO$_4$ Sensing Electrode. *Sens. Actuators, B* **2014,** *195*, 520-525.

(21) Anggraini, S. A.; Breedon, M.; Miura, N. Sensing Characteristics of Aged Zirconia-Based Hydrogen Sensor Utilizing Zn-Ta-Based Oxide Sensing-Electrode. *Electrochem. Commun.* **2013,** *31*, 133-136.

(22) Park, J.; Yoon, B. Y.; Park, C. O.; Lee, W.-J.; Lee, C. B. Sensing Behavior and Mechanism of Mixed Potential NO$_x$ Sensors Using NiO, NiO(+YSZ) and CuO Oxide Electrodes. *Sens. Actuators, B* **2009,** *135*, 516-523.

(23) Garzon, F. H.; Mukundan, R.; Brosha, E. L. Solid-State Mixed Potential Gas Sensors Theory, Experiments and Challenges. *Solid State Ionics* **2000,** *136-137*, 633-638.

(24) Zhu, T. L.; Fowler, D. E.; Poeppelmeier, K. R.; Han, M.; Barnett, S. A. Hydrogen Oxidation Mechanisms on Perovskite Solid Oxide Fuel Cell Anodes. *J. Electrochem. Soc.* **2016,** *163*, F952-F961.

(25) Danilovic, N.; Vincent, A.; Luo, J. L.; Chuang, K. T.; Hui, R.; Sanger, A. R. Correlation of Fuel Cell Anode Electrocatalytic and ex Situ Catalytic Activity of Perovskite La$_{0.75}$Sr$_{0.25}$Cr$_{0.5}$X$_{0.5}$O$_{3-\delta}$ (X = Ti, Mn, Fe, Co). *Chem. Mater.* **2010,** *22*, 957-965.

(26) Ross, J. R. H. *The Kinetics and Mechanisms of Catalytic Reactions, in: Heterogeneous Catalysis: Fundamentals and Applications*; Elsevier: Amsterdam,

2012; Chapter 6, pp 123-142.

(27) Tan, Y.; Tan, T. C. Characteristics and Modeling of a Solid-State Hydrogen Sensor. *J. Electrochem. Soc.* **1994,** *141*, 461-467.

(28) Breedon, M.; Miura, N. Augmenting H_2 Sensing Performance of YSZ-Based Electrochemical Gas Sensors via the Application of Au Mesh and YSZ Coating. *Sens. Actuators, B* **2013,** *182*, 40-44.

(29) Yamaguchi, M.; Anggraini, S. A.; Fujio, Y.; Sato, T.; Breedon, M.; Miura, N. Stabilized Zirconia-Based Sensor Utilizing SnO_2-Based Sensing Electrode with an Integrated Cr_2O_3 Catalyst Layer for Sensitive and Selective Detection of Hydrogen. *Int. J. Hydrogen Energy* **2013,** *38*, 305-312.

(30) Li, Y.; Li, X. G.; Tang, Z. Y; Tang, Z. N; Yu, J.; Wang, J. Hydrogen Sensing of the Mixed-Potential-Type $MnWO_4$/YSZ/Pt Sensor. *Sens. Actuators, B* **2015,** *206*, 176-180.

(31) Li, Y.; Li, X. G.; Tang, Z. Y; Wang, J.; Yu, J.; Tang, Z. N. Potentiometric Hydrogen Sensors Based on Yttria-Stabilized Zirconia Electrolyte (YSZ) and $CdWO_4$ Interface. *Sens. Actuators, B* **2016,** *223*, 365-371.

TOC